Letter

Floquet Weyl semimetal phases in light-irradiated higher-order topological Dirac semimetals

Zi-Ming Wang,[1,2] Rui Wang,[2,3] Jin-Hua Sun,[4,*] Ting-Yong Chen,[5,†] and Dong-Hui Xu[2,3,‡]

[1]*Department of Physics, Hubei University, Wuhan 430062, China*

[2]*Department of Physics and Chongqing Key Laboratory for Strongly Coupled Physics, Chongqing University, Chongqing 400044, China*

[3]*Center of Quantum Materials and Devices, Chongqing University, Chongqing 400044, China*

[4]*Department of Physics, Ningbo University, Ningbo 315211, China*

[5]*Shenzhen Institute for Quantum Science and Engineering, Southern University of Science and Technology, Shenzhen 518055, China*

(Received 6 October 2022; accepted 21 March 2023; published 29 March 2023)

Floquet engineering, the concept of tailoring a system by a periodic drive, is increasingly exploited to design and manipulate topological phases of matter. In this work we study periodically driven higher-order topological Dirac semimetals associated with a k-dependent quantized quadrupole moment by applying circularly polarized light. The undriven Dirac semimetals feature gapless higher-order hinge Fermi arc states which are the consequence of the higher-order topology of the Dirac nodes. Floquet Weyl semimetal phases with hybrid-order topology, characterized by both a k-dependent quantized quadrupole moment and a k-dependent Chern number, emerge when illumining circularly polarized light. Such Floquet Weyl semimetals support both hinge Fermi arc states and topological surface Fermi arc states. In addition, Floquet Weyl semimetals with tilted Weyl cones in higher-order topological Dirac semimetals are also discussed. Considering numerous higher-order topological Dirac semimetal materials were recently proposed, our findings can be testable soon.

DOI: 10.1103/PhysRevB.107.L121407

Introduction. Understanding Dirac-like fermions has become an imperative in modern condensed-matter physics. All across the research frontier, ranging from graphene to d-wave high-temperature superconductors to topological insulators and beyond, low-energy excitations in various electronic systems can be well described by the Dirac equation [1]. Of particular interest are Dirac semimetals (DSMs), as they represent an unusual phase of quantum matter that hosts massless Dirac fermions as quasiparticle excitations near bulk nodal points. Graphene is a well-known two-dimensional (2D) DSM protected by chiral (sublattice) symmetry [2], and stable three-dimensional (3D) DSMs protected by crystalline symmetries had been identified and realized in solid materials as well [3]. Due to the lack of bulk-boundary correspondence, the cornerstone of topological phases of matter, the designation of DSMs as a semimetallic topological phase was controversial [4,5], whereas DSMs do serve as a parent phase for realizing exotic topological states and topological phenomena. For instance, breaking time-reversal symmetry (TRS) via magnetism in a DSM can result in the quantum anomalous Hall state [6] or Weyl semimetal (WSM) states hosting massless chiral fermions and surface Fermi arc states [7].

Floquet engineering is a versatile approach that uses time-periodic driving of a quantum system to enable novel out-of-equilibrium many-body quantum states [8–10]. Recent years have witnessed intense efforts toward exploiting Floquet engineering to create topological phases in quantum materials [11–50]. It is important to stress that circularly polarized light (CPL) naturally breaks TRS, which provides an easy tuning knob to induce dynamical topological phases such as Floquet Chern insulators and Floquet WSMs in DSMs [16,17,19–23,36,39,42,51–53]. Following the discovery of the concept of higher-order topology that characterizes boundary states with dimensions two or more lower than that of the bulk system that accommodates them [54–60], there has been a surge of interest in tailoring higher-order topological phases by using Floquet engineering as well [61–78]. Meanwhile, numerous higher-order topological DSMs, which obey the topological bulk-hinge correspondence and thus display universal topological hinge Fermi arc states, have been proposed [79–84]. The signature of hinge Fermi arc states was recently observed in supercurrent oscillation experiments on prototypical DSM material Cd_3As_2 [85,86]. Cd_3As_2 provides a promising parent material for the realization of the higher-order WSM [87–89] that supports hinge Fermi arc states in addition to the usual surface Fermi arc states by using Floquet engineering.

In this work we explore tunable higher-order WSMs in time-symmetric and PT-symmetric higher-order topological DSMs under off-resonant CPL illumination. Without driving, both types of higher-order topological DSMs have two bulk Dirac nodes locating at the k_z axis and support gapless hinge Fermi arc states. Meanwhile, the time-symmetric one has additional closed-surface Fermi rings. CPL drives each Dirac node to split into a pair of Weyl nodes by symmetry breaking, resulting in Floquet higher-order WSMs accommodating rich topological boundary states. The coexistence of surface Fermi arc and hinge Fermi arc states signals a hybrid-order topology which can be captured by k-dependent quantized quadrupole moment and Chern number. In addition, the surface Fermi rings in the time-symmetric DSM are inherited in the Floquet WSM. Moreover, we can achieve a type-II higher-order WSM

*sunjinhua@nbu.edu.cn
†chenty@sustech.edu.cn
‡donghuixu@cqu.edu.cn

with overtilted Weyl cones by adjusting the incident direction of CPL. Our proposal can be realized in DSM materials like Cd_3As_2 with current ultrafast experimental techniques.

DSM model and the Floquet theory. Undriven higher-order topological DSMs are constructed based on a generic band inversion DSM model on the cubic lattice. In reciprocal space, the Hamiltonian matrix is

$$H(\boldsymbol{k}) = \epsilon_0(\mathbf{k}) + \lambda \sin k_x \Gamma_1 + \lambda \sin k_y \Gamma_2 + M(\mathbf{k})\Gamma_3 + G(\mathbf{k})\Gamma_4, \quad (1)$$

where the Γ matrices are $\Gamma_1 = s_3\sigma_1$, $\Gamma_2 = s_0\sigma_2$, $\Gamma_3 = s_0\sigma_3$, $\Gamma_4 = s_1\sigma_1$, and $\Gamma_5 = s_2\sigma_1$, with $s_{j=1,2,3}$ and $\sigma_{j=1,2,3}$ the Pauli matrices labeling the spin and orbital degrees of freedom, respectively, and s_0, σ_0 are 2×2 identity matrices. $\epsilon_0(\mathbf{k}) = t_1(\cos k_z - \cos K_z^0) + t_2(\cos k_x + \cos k_y - 2)$, and $M(\mathbf{k}) = t(\cos k_x + \cos k_y - 2) + t_z(\cos k_z - \cos K_z^0)$. $t_{1,2}$, t, t_z, and λ are the amplitudes of hoppings. The DSM has two Dirac points locating at $\mathbf{k}^0 = (0, 0, \pm K_z^0)$. $G(\mathbf{k})$ is the coefficient of the Γ_4 term that gives birth to higher-order topology in the present DSMs. Without the Γ_4 term, this model describes an ordinary band-inversion DSM supporting helical surface Fermi arc states which are not topologically stable [4]. Equation (1) can describe the recently identified higher-order DSM materials, including but not limited to Cd_3As_2 and KMgBi [80].

Treating k_z as a parameter, then $H(\mathbf{k})$ reduces to a 2D Hamiltonian $H_{k_z}(k_x, k_y)$. The reduced Hamiltonian possesses higher-order topology, which can be well characterized by the quantized quadrupole moment. Furthermore, we can use a k_z-dependent quantized quadrupole moment $\mathcal{Q}_{xy}(k_z)$ to capture the higher-order topology of the DSMs. $\mathcal{Q}_{xy}$ in real space [90,91] is

$$\mathcal{Q}_{xy} = \frac{1}{2\pi}\,\mathrm{Im}[\log\langle \hat{U}_{xy}\rangle], \quad \hat{U}_{xy} = e^{i2\pi\sum_{r_i}\hat{q}_{xy}(\boldsymbol{r}_i)}, \quad (2)$$

where $\hat{q}_{xy}(\boldsymbol{r}_i) = \frac{xy}{L_xL_y}\hat{n}(\boldsymbol{r}_i)$ is the quadrupole moment density per unit cell at site $\boldsymbol{r}_i$, and L_x and L_y are the length of the system in the x and y directions, respectively.

CPL is described by a time-periodic gauge field $\mathbf{A}(\tau) = \mathbf{A}(\tau + T)$ with period $T = \frac{2\pi}{\omega}$ and the frequency of light ω. Specifically, the gauge field $\mathbf{A} = A(0, \eta\sin\omega\tau, \cos\omega\tau)$, $A(\cos\omega\tau, 0, \eta\sin\omega\tau)$, and $A(\eta\sin\omega\tau, \cos\omega\tau, 0)$, with $\eta = \pm 1$ labeling the handedness, describe CPL propagating along the x, y, and z directions, respectively. In the main text we mainly focus on the case of CPL propagating along the z direction; the case of CPL propagating along the x direction is also studied in the Supplemental Material [103]. Electrons move on a lattice couple to the electromagnetic gauge field via the Peierls substitution: $\tilde{t} \to \tilde{t}\exp[-i\int_{\mathbf{r}_j}^{\mathbf{r}_k}\mathbf{A}(\tau)\cdot d\mathbf{r}]$, where $\mathbf{r}_j$ is the coordinate of lattice site j. Thereby, in the presence of CPL, the DSM Hamiltonian becomes periodic in time $H(\tau) = H(\tau + T)$. In the following we use the natural units $e = \hbar = c = 1$. Thanks to Floquet's theorem, we can transfer the time-dependent Hamiltonian problem to a time-independent one [92,93]. Specifically, the time-dependent Schrödinger equation has a set of solution $|\Psi(\tau)\rangle = e^{-i\epsilon\tau}|\Phi(\tau)\rangle$, where ϵ denotes the Floquet quasienergy, and $|\Phi(\tau)\rangle = |\Phi(\tau + T)\rangle$ is dubbed the Floquet state. Expanding the Floquet state in a Fourier series

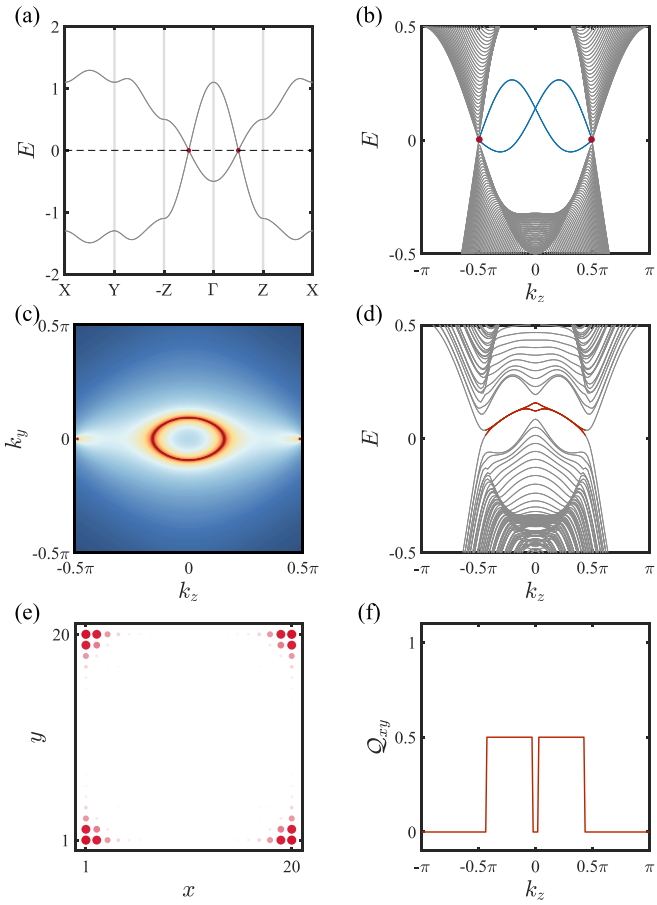

FIG. 1. Electronic structures and bulk topology of the time-symmetric DSM. (a) Bulk band structure along high-symmetry points in the 3D Brillouin zone. The red dots mark the bulk Dirac points. (b) The surface band dispersion vs k_z direction for $k_y = 0$. The open boundary condition (OBC) is imposed along the x direction. The solid blue lines show the gapless surface Dirac states. (c) The surface spectral function on the $k_y - k_z$ plane with the semi-infinite boundary along the x direction when $E = 0$. The red dots at $\pm\pi/2$ are the projection of Dirac points, and the red circle marks the surface Fermi rings from the surface Dirac states shown in (b). (d) The energy spectrum vs k_z with the OBC along both the x and y directions. The solid red lines represent the topologically protected hinge Fermi arc states. The Dirac points at $k_z = \pm\pi/2$ are gapped due to the size effect. (e) The local density of states (LDOS) of the hinge Fermi arc states at $k_z = 0.1\pi$. (f) The k_z-dependent quantized quadrupole moment $\mathcal{Q}_{xy}$. The two quantized plateaus of $\mathcal{Q}_{xy}$ correspond to two segments of degenerate hinge Fermi arc states. The parameters are chosen as $t_1 = 0.3, t_2 = 0.2, \lambda = 0.5, t = 1, t_z = 0.8, K_z^0 = \pi/2$, and $g = -0.4$.

$|\Phi(\tau)\rangle = \sum_n e^{-in\omega\tau}|\Phi^n\rangle$, we arrive at an infinite dimensional eigenvalue equation in the extended Hilbert (or Sambe) space,

$$\sum_m (H_{n-m} - m\omega\delta_{mn})\left|\Phi_\alpha^m\right\rangle = \epsilon_\alpha\left|\Phi_\alpha^m\right\rangle, \quad (3)$$

where $H_{n-m} = \frac{1}{T}\int_0^T d\tau e^{i(n-m)\omega\tau}H(\tau)$. Throughout, we focus on the case in the high-frequency limit, where the resonant interband transitions are very unlikely. This case yields an

effective static Floquet Hamiltonian [94,95]:

$$H_{\text{eff}} = H_0 + \sum_{l\neq 0} \frac{[H_{-l}, H_l]}{l\omega} + \mathcal{O}(\omega^{-2}). \tag{4}$$

In our calculations, the maximum value of l is determined by checking whether the results converge.

Light-irradiated time-symmetric higher-order topological DSM. First, we specify $G(\mathbf{k}) = g(\cos k_x - \cos k_y)\sin k_z$, which breaks the fourfold rotation symmetry $\mathcal{C}_{4z}$ but preserves TRS $\mathcal{T}$ and inversion symmetry $\mathcal{P}$, where $\mathcal{P} = \Gamma_3$ and $\mathcal{T} = is_2\mathcal{K}$, with $\mathcal{K}$ the complex conjugation. With the present form of $G(\mathbf{k})$, the Dirac points shown in Fig. 1(a) stay at the same position as the case without $G(\mathbf{k})$. Yet, the surface states behave quite differently. A closed Fermi ring, instead of helical Fermi arc states [Fig. 1(c)], emerges in the surface Brillouin zone [4] when the Fermi energy cuts through the surface Dirac cone [see the band crossing around $k_z = 0$ marked in blue in Fig. 1(b)]. More importantly, the DSM is endowed with the higher-order topology characterized by $\mathcal{Q}_{xy}(k_z)$ shown in Fig. 1(f). Note that $G(k_x, k_y, k_z = 0) = 0$ due to explicit dependence of $\sin k_z$, which results in a vanishing $\mathcal{Q}_{xy}$ within a small window around $k_z = 0$ for a finite-size system. Quantized $\mathcal{Q}_{xy}$ leads to topological hinge Fermi arcs terminated by the projection of the Dirac points, as shown in Figs. 1(d) and 1(e). Recently, the evidence of hinge Fermi arc states was experimentally reported in DSM Cd_3As_2 [85,86], which might be attributed to the existence of this type of $G(\mathbf{k})$.

In the presence of CPL propagating along the z direction, we obtain an effective Floquet Hamiltonian according to Eq. (4):

$$\begin{aligned} H^{\text{I}}_{\text{eff}}(\boldsymbol{k}) = {} & \left[t_1\left(\cos k_z - \cos K_z^0\right) + t_2\mathcal{J}_0(A)(\cos k_x + \cos k_y) - 2t_2\right] + \lambda\mathcal{J}_0(A)(\sin k_x\Gamma_1 + \sin k_y\Gamma_2) + \mathcal{J}_0(A)G(k)\Gamma_4 \\ & + \left[t_z\left(\cos k_z - \cos K_z^0\right) + t\mathcal{J}_0(A)(\cos k_x + \cos k_y) - 2t\right]\Gamma_3 + \sum_{l>0, l\in odd} \frac{4\eta\mathcal{J}_l^2(A)}{l\hbar\omega}\{\lambda^2\cos k_x\cos k_y\Gamma_{12} \\ & - \lambda t[\cos k_x\sin k_y\Gamma_{13} - \sin k_x\cos k_y\Gamma_{23}] + \lambda g\sin k_z[\cos k_x\sin k_y\Gamma_{14} - \sin k_x\cos k_y\Gamma_{24}] \\ & + 2tg\sin k_x\sin k_y\sin k_z\Gamma_{34}\}, \end{aligned} \tag{5}$$

where $\mathcal{J}_l(A)$ is the Bessel function of lth order and of the first kind, $\Gamma_{jk} = [\Gamma_j, \Gamma_k]/2i$. Equation (5) indicates that CPL not only renormalizes electron hopping perpendicular to the propagation direction but also induces TRS breaking hopping terms. Notably, each Dirac point is separated into a pair of Weyl points, resulting in a Floquet WSM with two pairs of Weyl nodes. The Floquet WSM hosts surface Fermi arc states around the original Dirac points, which connect the projection of each single pair of Weyl nodes as depicted in Figs. 2(a)–2(d). Note that electron pockets are formed around the projection of two of the four Weyl points, because each pair of Weyl nodes is separated in energy [see the zoom-in plots in Figs. 2(b) and 2(d)]. As depicted in Figs. 2(a) and 2(c), the WSM also supports the closed-surface Fermi ring generated by surface Dirac states, as does the undriven DSM. Coexistence of Fermi arcs and Fermi rings on the surface of time-reversal invariant WSM had been revealed in Ref. [96]. In our case, TRS is broken in the Floquet WSM; however, the coexisting Fermi arcs and Fermi ring are still present. Moreover, the Floquet WSM also features the hinge Fermi arc states terminated by the projection of two adjacent Weyl nodes from two different pairs [Fig. 2(e)]. To capture the topology of the Floquet WSM, in Fig. 2(f) we show the quantized quadrupole moment and the Chern number as functions of k_z. We can see that the quadrupole moment takes a quantized value of $\mathcal{Q}_{xy} = 1/2$ in between the two middle Weyl points, and the Chern number displays $\mathcal{C}_n = 1$ between the same pairs of Weyl nodes.

The Dirac points in Cd_3As_2 come from the band crossing induced by band inversion. The characteristic low-energy scale describing the band inversion is about 50 meV [97,98]. We notice the pump photon energy in a recent experiment on Floquet band engineering can reach 440 meV [99]. Therefore the implementation of CPL at high frequency is feasible in such a Dirac semimetal material.

Light-irradiated PT-symmetric higher-order topological DSM. We consider $G(\mathbf{k})$ is independent of k_z, i.e., $G(\mathbf{k}) = g(\cos k_x - \cos k_y)$, it also generates higher-order topology in the DSM. The previously defined TRS is broken; however, the system still has two fourfold degenerate Dirac points [Fig. 3(a)], which is called PT-symmetric DSM as the combination of TRS and inversion symmetry $\mathcal{P}\otimes\mathcal{T} = is_2\sigma_2\mathcal{K}$ is preserved. It is still of interest to ask whether CPL induces intriguing Floquet topological states as it does in the time-symmetric DSM. Before going into the Floquet states, it's better to take a look at the electronic structure of the DSM. From Fig. 3 we can see that, in contrast to the time-symmetric type DSM, the surface states in PT-symmetric DSM are separated and no surface Dirac cones exist [Figs. 3(b) and 3(c)]. Still, it supports gapless hinge Fermi arc states terminated on the projection of two Dirac points, as shown in Figs. 3(d) and 3(e). Moreover, in Fig. 3(f) we calculate $\mathcal{Q}_{xy}(k_z)$ to capture the higher-order topology of this type of DSM. Such a type of higher-order topological DSM can be realized in antiferromagnetic systems, as the present Γ_4 term may represent an orbital-dependent spin-density wave. Under the high-frequency CPL along the z direction, we also obtain an effective Floquet Hamiltonian for the PT-symmetric higher-order topological DSM, which can be considered as a special case of Eq. (5) where $\sin k_z = 1$. Similarly, CPL renormalizes the original hoppings and also induces the next-nearest-neighbor hoppings on the $x-y$ plane, which breaks

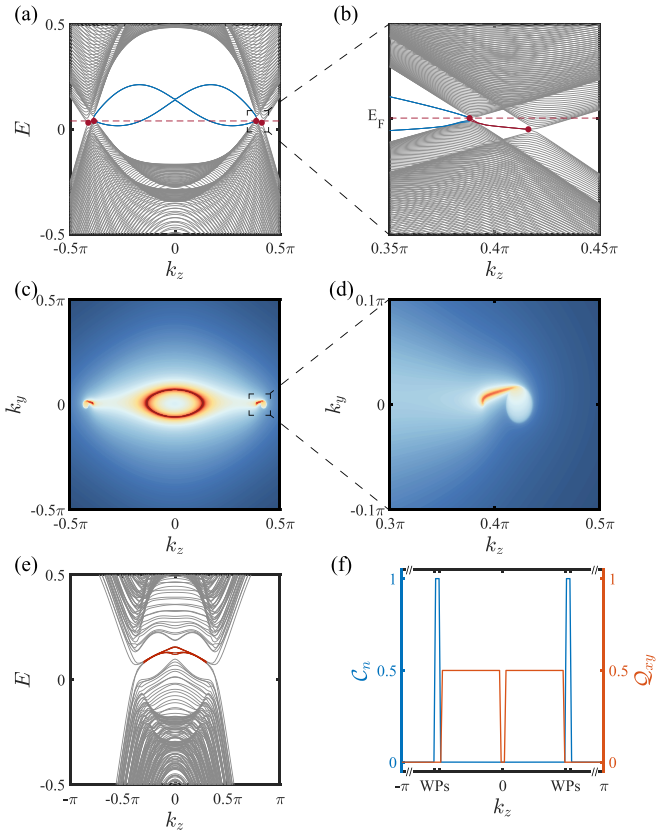

FIG. 2. The electronic structure and bulk topology of the Floquet WSM in the light-irradiated time-symmetric DSM. (a) The surface band structure vs k_z for $k_y = 0$. (b) The zoom-in view of the area around the pair of Weyl points within the black dashed square in (a). The red dots show the Weyl points, and the red solid lines represent the surface Fermi arc states. (c) The surface spectral function on the $k_y - k_z$ plane with the semi-infinite boundary along the x direction at E_F marked in red dashed line in (b). The red solid lines around the original Dirac points mark the surface Fermi arcs, which connect the same pair of Weyl points. The red closed circle shows the surface Fermi rings. (d) The zoom-in view of the surface Fermi arc within the black dashed square in (c). The shaded area connecting the right end of the Fermi arc marks the electron pocket. (e) The energy spectrum as a function of k_z for the OBC along the x and y directions. The hinge states are marked by the solid red lines. (f) $\mathcal{Q}_{xy}$ and the Chern number $\mathcal{C}_n$ marked in orange and blue, respectively, as functions of k_z. The parameters are the same as those in Fig. 1, except $A = 0.7$ and $\omega = 3$.

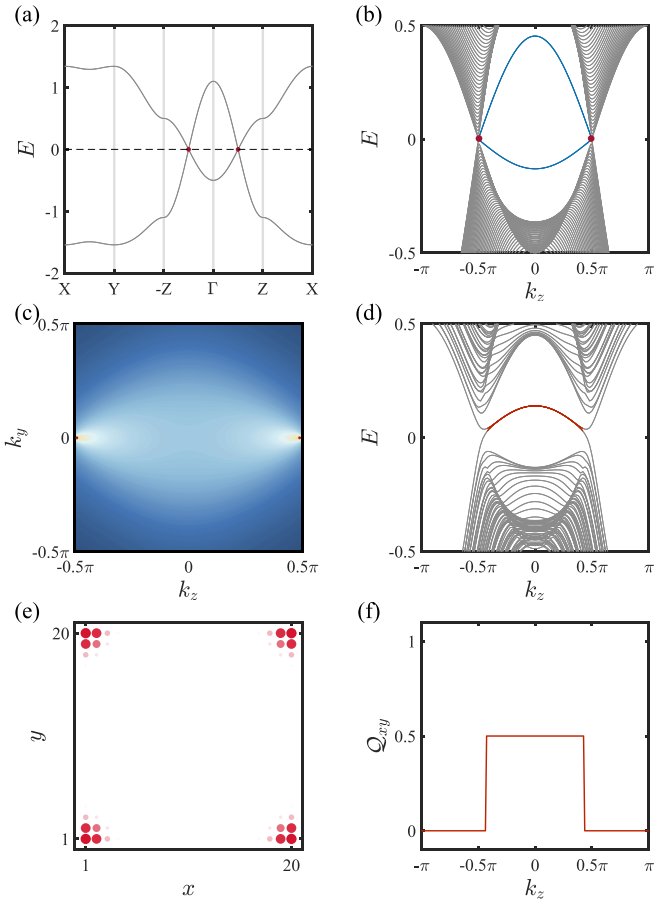

FIG. 3. The energy spectrum and bulk topology of the PT-symmetric DSM. (a) Band structure along high-symmetry points in the 3D Brillouin zone. (b) The surface band structure vs k_z direction for $k_y = 0$. The blue solid lines show the separable surface state between two Dirac points marked in red dots. (c) The surface spectral function on the $k_y - k_z$ plane with the semi-infinite boundary along the x axis when $E = 0$. The red dots are the projection of two Dirac points. (d) The energy spectrum vs k_z for the OBC along both the x and y directions. The solid red lines represent the topologically protected hinge Fermi arc states. (e) The LDOS of the hinge Fermi arc states at $k_z = 0.1\pi$. (f) The k_z-dependent quantized quadrupole moment $\mathcal{Q}_{xy}$. $\mathcal{Q}_{xy}$ shows a quantized plateau where the hinge Fermi arc marked in (d) exists. The parameters are chosen as $t_1 = 0.3$, $t_2 = 0.2$, $\lambda = 0.5$, $t = 1$, $t_z = 0.8$, $K_z^0 = \pi/2$, and $g = -0.4$.

$\mathcal{P} \otimes \mathcal{T}$. Accordingly, each Dirac point splits into a pair of Weyl points along the k_z direction in reciprocal space. Interestingly, the two middle Weyl points from two different pairs are connected by two separable surface-state bands [see the solid blue lines in Fig. 4(a)], while the two Weyl points within the same pair evolved from the same Dirac point are connected by surface Fermi arc states, as displayed in Figs. 4(b), 4(c), and 4(d). Just like in the light-irradiated time-symmetric DSM, the surface Fermi arc states are also terminated by the projection of a Weyl node and an electron pocket. The emergence of the Fermi arc states is attributed to a k-dependent $\mathcal{C}_n$ plotted in Fig. 4(f). In addition, as shown in Fig. 4(e), gapless hinge Fermi arc states exist between the two middle Weyl points, whose higher-order topology can also be characterized by $\mathcal{Q}_{xy}(k_z)$ demonstrated in Fig. 4(f).

Tilting effect on the Floquet WSM. KMgBi was identified as a critically tilted DSM [100] with higher-order topology [80] that is believed to be caused by $G(\mathbf{k}) = g(\cos k_x - \cos k_y) \sin k_z$. Strain or chemical doping can change the tilt of Dirac cones and drive the DSM into a phase with type-II (i.e., overtilted) [101,102] Dirac cones. The transition between type-I and type-II Dirac cones is determined by the ratio of $|t_1/t_z|$ in Eq. (1). For overtilted Dirac cones with $|t_1/t_z| > 1$, shining CPL can also create Floquet WSM states. Figure 5 shows the Floquet WSM in the CPL-illuminated time-symmetric DSM with tilted Dirac cones. When $|t_1/t_z| = 1$, the DSM is at the critical point between the type-I and

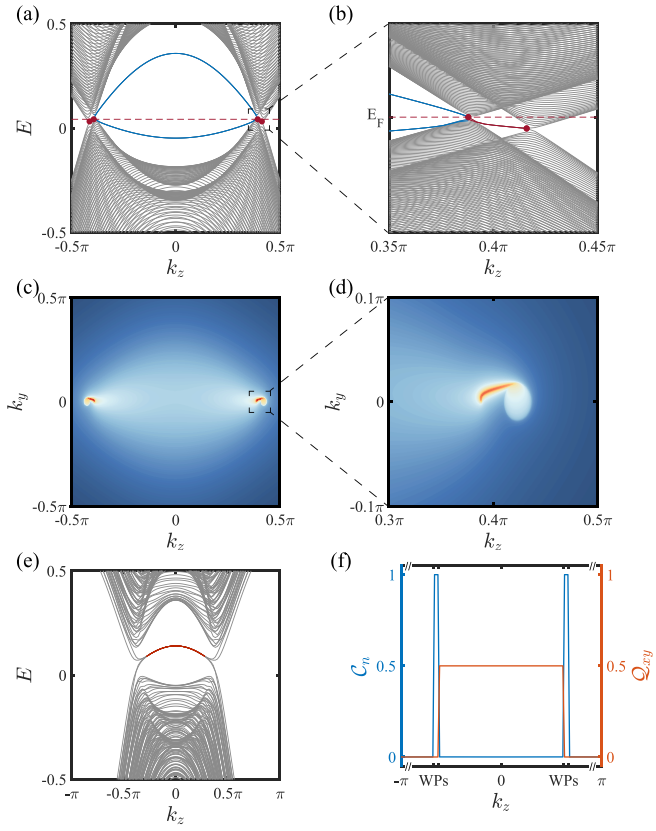

FIG. 4. The electronic structure and bulk topology of the Floquet WSM in the light-irradiated PT-symmetric DSM. (a) The surface band structure along k_z direction when $k_y = 0$. The blue solid lines show the separable surface state between the two middle of Weyl points marked in red dots. (b) The zoom-in view of the area around the pair of Weyl points within the black dashed square in (a). The red solid lines represent the surface Fermi arc states. (c) The surface spectral function on the $k_y - k_z$ plane with the semi-infinite boundary along the x direction at E_F marked by red dashed line in (b). The red lines around the original Dirac points show the surface Fermi arc states, which connect the same pair of Weyl points. The zoom-in view of the surface Fermi arc within the black dashed square in (c). The shaded area attached to the right end of the Fermi arc marks the electron pocket. (e) The energy spectrum as a function of k_z for the OBC along the x and y directions. (f) $\mathcal{Q}_{xy}$ and $\mathcal{C}_n$ marked in orange and blue, respectively, as functions of k_z. The parameters are the same as those in Fig. 2.

type-II DSMs. Accordingly, a critical type of Floquet WSM is obtained as shown in Fig. 5(a). When $|t_1/t_z| > 1$, a type-II Floquet WSM appears by applying CPL. In this case, electron and hole pockets meet at the Weyl points [Fig. 5(b)]. From Figs. 5(c)–5(f) we can see that the type-II WSM also hosts surface Dirac states, surface Fermi arc states, as well as hinge Fermi arc states; however, these boundary states are deeply buried in the bulk states.

At last, we would like to briefly discuss how the Floquet WSM responds to change in propagation orientation of CPL. Applied CPL propagating along the x direction can also induce Floquet WSM states in higher-order topological DSMs. In the Supplemental Material [103], we show that starting

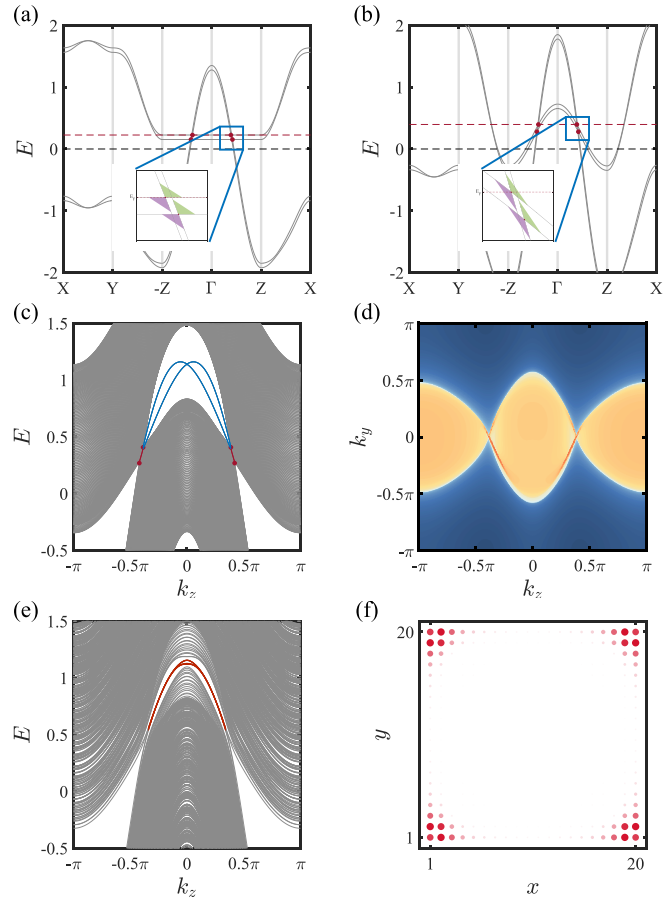

FIG. 5. The energy spectrum of tilted Floquet WSMs. (a) Bulk band structure of the critical type of WSM along the high-symmetry points in the 3D Brillouin zone. The four red dots mark the Weyl nodes. The inset is a zoom of a pair of Weyl nodes. The green and purple triangles in the inset represent the conduction band and valence band, respectively. (b) The bulk band of the type-II WSM with $t_1 = 1.3$ and $|t_1/t_z| > 1$. (c) The surface band structure along k_z direction when $k_y = 0$. The solid blue lines show the gapless surface Dirac states, and red lines are the surface Fermi arc states between pairs of Weyl nodes. (d) The surface spectral function on the $k_y - k_z$ plane with the OBC along the x axis when $E = 0.29$. The electron and hole pockets are marked by yellow shaded regions. The red curves are the surface Fermi arcs. (e) The energy spectrum vs k_z for the OBC along the x and y directions. The red solid lines represent the hinge Fermi arc state. (f) The LDOS of the hinge Fermi arc state at $k_z = 0.1\pi$. The parameters are chosen to be $t_2 = 0.2, \lambda = 0.5, t = 1, t_z = 0.8, K_z^0 = \pi/2, g = -0.4, A = 0.7$, and $\omega = 3$.

with a time-symmetric higher-order topological DSM with type-I Dirac cone, the CPL along the x direction can induce a Floquet WSM with overtilted type-II Weyl cones. This implies that the type of Floquet WSMs can be tuned by adjusting the propagation direction of incident light.

Conclusions. In this work we have investigated the CPL-induced Floquet WSM states in both time-symmetric and PT-symmetric higher-order topological DSMs. The emergent Floquet WSM states exhibit higher-order topological hinge Fermi arc states characterized by a k-dependent

quadrupole moment. Moreover, the Floquet WSMs show gapless Fermi arc states whose topologies are characterized by a k-dependent Chern number. Our work not only reveals exotic hybrid-order topological WSM states but also suggests an approach to realizing such WSMs in solids rather than acoustic systems [104,105].

Acknowledgments. The authors acknowledge support by the NSFC (under Grants No. 12074108, No. 12222402, and No. 12147102), the Natural Science Foundation of Chongqing (Grant No. CSTB2022NSCQ-MSX0568), as well as Shenzhen Institute for Quantum Science and Engineering (under Grant No. SIQSE202101).

[1] O. Vafek and A. Vishwanath, Dirac fermions in solids: From high-T_c cuprates and graphene to topological insulators and Weyl semimetals, Annu. Rev. Condens. Matter Phys. **5**, 83 (2014).

[2] A. H. Castro Neto, F. Guinea, N. M. R. Peres, K. S. Novoselov, and A. K. Geim, The electronic properties of graphene, Rev. Mod. Phys. **81**, 109 (2009).

[3] N. P. Armitage, E. J. Mele, and A. Vishwanath, Weyl and Dirac semimetals in three-dimensional solids, Rev. Mod. Phys. **90**, 015001 (2018).

[4] M. Kargarian, M. Randeria, and Y.-M. Lu, Are the surface Fermi arcs in Dirac semimetals topologically protected? Proc. Natl. Acad. Sci. USA **113**, 8648 (2016).

[5] B. J. Wieder, B. Bradlyn, J. Cano, Z. Wang, M. G. Vergniory, L. Elcoro, A. A. Soluyanov, C. Felser, T. Neupert, N. Regnault *et al.*, Topological materials discovery from crystal symmetry, Nat. Rev. Mater. **7**, 196 (2022).

[6] F. D. M. Haldane, Model for a Quantum Hall Effect without Landau Levels: Condensed-Matter Realization of the "Parity Anomaly," Phys. Rev. Lett. **61**, 2015 (1988).

[7] X. Wan, A. M. Turner, A. Vishwanath, and S. Y. Savrasov, Topological semimetal and Fermi-arc surface states in the electronic structure of pyrochlore iridates, Phys. Rev. B **83**, 205101 (2011).

[8] A. Eckardt, Colloquium: Atomic quantum gases in periodically driven optical lattices, Rev. Mod. Phys. **89**, 011004 (2017).

[9] A. dela Torre, D. M. Kennes, M. Claassen, S. Gerber, J. W. McIver, and M. A. Sentef, Colloquium: Nonthermal pathways to ultrafast control in quantum materials, Rev. Mod. Phys. **93**, 041002 (2021).

[10] C. Weitenberg and J. Simonet, Tailoring quantum gases by Floquet engineering, Nat. Phys. **17**, 1342 (2021).

[11] J. Cayssol, B. Dóra, F. Simon, and R. Moessner, Floquet topological insulators, Phys. Status Solidi RRL **7**, 101 (2013).

[12] T. Oka and S. Kitamura, Floquet engineering of quantum materials, Annu. Rev. Condens. Matter Phys. **10**, 387 (2019).

[13] F. Harper, R. Roy, M. S. Rudner, and S. Sondhi, Topology and broken symmetry in Floquet systems, Annu. Rev. Condens. Matter Phys. **11**, 345 (2020).

[14] M. S. Rudner and N. H. Lindner, Band structure engineering and non-equilibrium dynamics in Floquet topological insulators, Nat. Rev. Phys. **2**, 229 (2020).

[15] C. Bao, P. Tang, D. Sun, and S. Zhou, Light-induced emergent phenomena in 2D materials and topological materials, Nat. Rev. Phys. **4**, 33 (2022).

[16] T. Oka and H. Aoki, Photovoltaic Hall effect in graphene, Phys. Rev. B **79**, 081406(R) (2009).

[17] J.-i. Inoue and A. Tanaka, Photoinduced Transition between Conventional and Topological Insulators in Two-Dimensional Electronic Systems, Phys. Rev. Lett. **105**, 017401 (2010).

[18] T. Kitagawa, E. Berg, M. Rudner, and E. Demler, Topological characterization of periodically driven quantum systems, Phys. Rev. B **82**, 235114 (2010).

[19] Z. Gu, H. A. Fertig, D. P. Arovas, and A. Auerbach, Floquet Spectrum and Transport through an Irradiated Graphene Ribbon, Phys. Rev. Lett. **107**, 216601 (2011).

[20] T. Kitagawa, T. Oka, A. Brataas, L. Fu, and E. Demler, Transport properties of nonequilibrium systems under the application of light: Photoinduced quantum Hall insulators without Landau levels, Phys. Rev. B **84**, 235108 (2011).

[21] P. Delplace, A. Gómez-León, and G. Platero, Merging of Dirac points and Floquet topological transitions in ac-driven graphene, Phys. Rev. B **88**, 245422 (2013).

[22] L. E. F. Foa Torres, P. M. Perez-Piskunow, C. A. Balseiro, and G. Usaj, Multiterminal Conductance of a Floquet Topological Insulator, Phys. Rev. Lett. **113**, 266801 (2014).

[23] G. Usaj, P. M. Perez-Piskunow, L. E. F. Foa Torres, and C. A. Balseiro, Irradiated graphene as a tunable Floquet topological insulator, Phys. Rev. B **90**, 115423 (2014).

[24] N. H. Lindner, G. Refael, and V. Galitski, Floquet topological insulator in semiconductor quantum wells, Nat. Phys. **7**, 490 (2011).

[25] T. Kitagawa, M. S. Rudner, E. Berg, and E. Demler, Exploring topological phases with quantum walks, Phys. Rev. A **82**, 033429 (2010).

[26] N. H. Lindner, D. L. Bergman, G. Refael, and V. Galitski, Topological Floquet spectrum in three dimensions via a two-photon resonance, Phys. Rev. B **87**, 235131 (2013).

[27] L. Jiang, T. Kitagawa, J. Alicea, A. R. Akhmerov, D. Pekker, G. Refael, J. I. Cirac, E. Demler, M. D. Lukin, and P. Zoller, Majorana Fermions in Equilibrium and in Driven Cold-Atom Quantum Wires, Phys. Rev. Lett. **106**, 220402 (2011).

[28] M. S. Rudner, N. H. Lindner, E. Berg, and M. Levin, Anomalous Edge States and the Bulk-Edge Correspondence for Periodically Driven Two-Dimensional Systems, Phys. Rev. X **3**, 031005 (2013).

[29] M. Ezawa, Photoinduced Topological Phase Transition and a Single Dirac-Cone State in Silicene, Phys. Rev. Lett. **110**, 026603 (2013).

[30] A. Gómez-León and G. Platero, Floquet-Bloch Theory and Topology in Periodically Driven Lattices, Phys. Rev. Lett. **110**, 200403 (2013).

[31] A. G. Grushin, A. Gómez-León, and T. Neupert, Floquet Fractional Chern Insulators, Phys. Rev. Lett. **112**, 156801 (2014).

[32] R. Wang, B. Wang, R. Shen, L. Sheng, and D. Y. Xing, Floquet Weyl semimetal induced by off-resonant light, Europhys. Lett. **105**, 17004 (2014).

[33] A. Narayan, Tunable point nodes from line-node semimetals via application of light, Phys. Rev. B **94**, 041409(R) (2016).

[34] Z. Yan and Z. Wang, Tunable Weyl Points in Periodically Driven Nodal Line Semimetals, Phys. Rev. Lett. **117**, 087402 (2016).

[35] K. Taguchi, D.-H. Xu, A. Yamakage, and K. T. Law, Photovoltaic anomalous Hall effect in line-node semimetals, Phys. Rev. B **94**, 155206 (2016).

[36] J. González and R. A. Molina, Macroscopic Degeneracy of Zero-Mode Rotating Surface States in 3D Dirac and Weyl Semimetals under Radiation, Phys. Rev. Lett. **116**, 156803 (2016).

[37] A. Narayan, Floquet dynamics in two-dimensional semi-Dirac semimetals and three-dimensional Dirac semimetals, Phys. Rev. B **91**, 205445 (2015).

[38] K. Saha, Photoinduced Chern insulating states in semi-Dirac materials, Phys. Rev. B **94**, 081103(R) (2016).

[39] C.-K. Chan, Y.-T. Oh, J. H. Han, and P. A. Lee, Type-II Weyl cone transitions in driven semimetals, Phys. Rev. B **94**, 121106(R) (2016).

[40] Z. Yan and Z. Wang, Floquet multi-Weyl points in crossing-nodal-line semimetals, Phys. Rev. B **96**, 041206(R) (2017).

[41] J.-Y. Zou and B.-G. Liu, Floquet Weyl fermions in three-dimensional stacked graphene systems irradiated by circularly polarized light, Phys. Rev. B **93**, 205435 (2016).

[42] H. Hübener, M. A. Sentef, U. De Giovannini, A. F. Kemper, and A. Rubio, Creating stable Floquet–Weyl semimetals by laser-driving of 3D Dirac materials, Nat. Commun. **8**, 13940 (2017).

[43] R. Chen, B. Zhou, and D.-H. Xu, Floquet Weyl semimetals in light-irradiated type-II and hybrid line-node semimetals, Phys. Rev. B **97**, 155152 (2018).

[44] D. Zhang, H. Wang, J. Ruan, G. Yao, and H. Zhang, Engineering topological phases in the Luttinger semimetal α-Sn, Phys. Rev. B **97**, 195139 (2018).

[45] SK Firoz Islam and A. A. Zyuzin, Photoinduced interfacial chiral modes in threefold topological semimetal, Phys. Rev. B **100**, 165302 (2019).

[46] T. Deng, B. Zheng, F. Zhan, J. Fan, X. Wu, and R. Wang, Photoinduced Floquet mixed-Weyl semimetallic phase in a carbon allotrope, Phys. Rev. B **102**, 201105(R) (2020).

[47] A. K. Ghosh, T. Nag, and A. Saha, Systematic generation of the cascade of anomalous dynamical first- and higher-order modes in Floquet topological insulators, Phys. Rev. B **105**, 115418 (2022).

[48] T. Nag and B. Roy, Anomalous and normal dislocation modes in Floquet topological insulators, Commun. Phys. **4**, 157 (2021).

[49] T. Nag, R.-J. Slager, T. Higuchi, and T. Oka, Dynamical synchronization transition in interacting electron systems, Phys. Rev. B **100**, 134301 (2019).

[50] X.-L. Du, R. Chen, R. Wang, and D.-H. Xu, Weyl nodes with higher-order topology in an optically driven nodal-line semimetal, Phys. Rev. B **105**, L081102 (2022).

[51] T. V. Trevisan, P. V. Arribi, O. Heinonen, R.-J. Slager, and P. P. Orth, Bicircular Light Floquet Engineering of Magnetic Symmetry and Topology and its Application to the Dirac Semimetal Cd_3As_2, Phys. Rev. Lett. **128**, 066602 (2022).

[52] Y. H. Wang, H. Steinberg, P. Jarillo-Herrero, and N. Gedik, Observation of Floquet-Bloch states on the surface of a topological insulator, Science **342**, 453 (2013).

[53] J. W. McIver, B. Schulte, F.-U. Stein, T. Matsuyama, G. Jotzu, G. Meier, and A. Cavalleri, Light-induced anomalous Hall effect in graphene, Nat. Phys. **16**, 38 (2020).

[54] F. Zhang, C. L. Kane, and E. J. Mele, Surface State Magnetization and Chiral Edge States on Topological Insulators, Phys. Rev. Lett. **110**, 046404 (2013).

[55] W. A. Benalcazar, B. A. Bernevig, and T. L. Hughes, Quantized electric multipole insulators, Science **357**, 61 (2017).

[56] J. Langbehn, Y. Peng, L. Trifunovic, F. von Oppen, and P. W. Brouwer, Reflection-Symmetric Second-Order Topological Insulators and Superconductors, Phys. Rev. Lett. **119**, 246401 (2017).

[57] Z. Song, Z. Fang, and C. Fang, $(d-2)$-Dimensional Edge States of Rotation Symmetry Protected Topological States, Phys. Rev. Lett. **119**, 246402 (2017).

[58] F. Schindler, A. M. Cook, M. G. Vergniory, Z. Wang, S. S. P. Parkin, B. A. Bernevig, and T. Neupert, Higher-order topological insulators, Sci. Adv. **4**, eaat0346 (2018).

[59] R. Chen, C.-Z. Chen, J.-H. Gao, B. Zhou, and D.-H. Xu, Higher-Order Topological Insulators in Quasicrystals, Phys. Rev. Lett. **124**, 036803 (2020).

[60] B. Xie, H.-X. Wang, X. Zhang, P. Zhan, J.-H. Jiang, M. Lu, and Y. Chen, Higher-order band topology, Nat. Rev. Phys. **3**, 520 (2021).

[61] R. W. Bomantara, L. Zhou, J. Pan, and J. Gong, Coupled-wire construction of static and Floquet second-order topological insulators, Phys. Rev. B **99**, 045441 (2019).

[62] M. Rodriguez-Vega, A. Kumar, and B. Seradjeh, Higher-order Floquet topological phases with corner and bulk bound states, Phys. Rev. B **100**, 085138 (2019).

[63] T. Nag, V. Juričić, and B. Roy, Out of equilibrium higher-order topological insulator: Floquet engineering and quench dynamics, Phys. Rev. Res. **1**, 032045(R) (2019).

[64] R. Seshadri, A. Dutta, and D. Sen, Generating a second-order topological insulator with multiple corner states by periodic driving, Phys. Rev. B **100**, 115403 (2019).

[65] Y. Peng and G. Refael, Floquet Second-Order Topological Insulators from Nonsymmorphic Space-Time Symmetries, Phys. Rev. Lett. **123**, 016806 (2019).

[66] H. Hu, B. Huang, E. Zhao, and W. V. Liu, Dynamical Singularities of Floquet Higher-Order Topological Insulators, Phys. Rev. Lett. **124**, 057001 (2020).

[67] A. K. Ghosh, G. C. Paul, and A. Saha, Higher order topological insulator via periodic driving, Phys. Rev. B **101**, 235403 (2020).

[68] Y. Peng, Floquet higher-order topological insulators and superconductors with space-time symmetries, Phys. Rev. Res. **2**, 013124 (2020).

[69] R. W. Bomantara, Time-induced second-order topological superconductors, Phys. Rev. Res. **2**, 033495 (2020).

[70] B. Huang and W. V. Liu, Floquet Higher-Order Topological Insulators with Anomalous Dynamical Polarization, Phys. Rev. Lett. **124**, 216601 (2020).

[71] W. Zhu, Y. D. Chong, and J. Gong, Floquet higher-order topological insulator in a periodically driven bipartite lattice, Phys. Rev. B **103**, L041402 (2021).

[72] R.-X. Zhang and Z.-C. Yang, Tunable fragile topology in Floquet systems, Phys. Rev. B **103**, L121115 (2021).

[73] T. Nag, V. Juričić, and B. Roy, Hierarchy of higher-order Floquet topological phases in three dimensions, Phys. Rev. B **103**, 115308 (2021).

[74] W. Zhu, Y. D. Chong, and J. Gong, Symmetry analysis of anomalous Floquet topological phases, Phys. Rev. B **104**, L020302 (2021).

[75] W. Zhu, M. Umer, and J. Gong, Floquet higher-order Weyl and nexus semimetals, Phys. Rev. Res. **3**, L032026 (2021).

[76] W. B. Rui, S.-B. Zhang, M. M. Hirschmann, Z. Zheng, A. P. Schnyder, B. Trauzettel, and Z. D. Wang, Higher-order Weyl superconductors with anisotropic Weyl-point connectivity, Phys. Rev. B **103**, 184510 (2021).

[77] B.-Q. Wang, H. Wu, and J.-H. An, Engineering exotic second-order topological semimetals by periodic driving, Phys. Rev. B **104**, 205117 (2021).

[78] S. Ghosh, K. Saha, and K. Sengupta, Hinge-mode dynamics of periodically driven higher-order Weyl semimetals, Phys. Rev. B **105**, 224312 (2022).

[79] M. Lin and T. L. Hughes, Topological quadrupolar semimetals, Phys. Rev. B **98**, 241103(R) (2018).

[80] B. J. Wieder, Z. Wang, J. Cano, X. Dai, L. M. Schoop, B. Bradlyn, and B. A. Bernevig, Strong and fragile topological Dirac semimetals with higher-order Fermi arcs, Nat. Commun. **11**, 627 (2020).

[81] Y. Fang and J. Cano, Classification of Dirac points with higher-order Fermi arcs, Phys. Rev. B **104**, 245101 (2021).

[82] A. C. Tyner, S. Sur, Q. Zhou, D. Puggioni, P. Darancet, J. M. Rondinelli, and P. Goswami, Quantized non-Abelian, Berry's flux and higher-order topology of Na_3Bi, arXiv:2102.06207.

[83] S. Nie, J. Chen, C. Yue, C. Le, D. Yuan, Z. Wang, W. Zhang, and H. Weng, Tunable Dirac semimetals with higher-order Fermi arcs in Kagome lattices $Pd_3Pb_2X_2$ (X = S, Se), Sci. Bull. **67**, 1958 (2022).

[84] X.-T. Zeng, Z. Chen, C. Chen, B.-B. Liu, X.-L. Sheng, and S. A. Yang, Topological hinge modes in Dirac semimetals, Front. Phys. **18**, 13308 (2023).

[85] C.-Z. Li, A.-Q. Wang, C. Li, W.-Z. Zheng, A. Brinkman, D.-P. Yu, and Z.-M. Liao, Reducing Electronic Transport Dimension to Topological Hinge States by Increasing Geometry Size of Dirac Semimetal Josephson Junctions, Phys. Rev. Lett. **124**, 156601 (2020).

[86] A.-Q. Wang, P.-Z. Xiang, T.-Y. Zhao, and Z.-M. Liao, Topological nature of higher-order hinge states revealed by spin transport, Sci. Bull. **67**, 788 (2022).

[87] H.-X. Wang, Z.-K. Lin, B. Jiang, G.-Y. Guo, and J.-H. Jiang, Higher-Order Weyl Semimetals, Phys. Rev. Lett. **125**, 146401 (2020).

[88] S. A. A. Ghorashi, T. Li, and T. L. Hughes, Higher-Order Weyl Semimetals, Phys. Rev. Lett. **125**, 266804 (2020).

[89] B. Roy, Antiunitary symmetry protected higher-order topological phases, Phys. Rev. Res. **1**, 032048(R) (2019).

[90] W. A. Wheeler, L. K. Wagner, and T. L. Hughes, Many-body electric multipole operators in extended systems, Phys. Rev. B **100**, 245135 (2019).

[91] B. Kang, K. Shiozaki, and G. Y. Cho, Many-body order parameters for multipoles in solids, Phys. Rev. B **100**, 245134 (2019).

[92] J. H. Shirley, Solution of the Schrödinger equation with a Hamiltonian periodic in time, Phys. Rev. **138**, B979 (1965).

[93] H. Sambe, Steady states and quasienergies of a quantum-mechanical system in an oscillating field, Phys. Rev. A **7**, 2203 (1973).

[94] M. Bukov, L. D'Alessio, and A. Polkovnikov, Universal high-frequency behavior of periodically driven systems: From dynamical stabilization to Floquet engineering, Adv. Phys. **64**, 139 (2015).

[95] A. Eckardt and E. Anisimovas, High-frequency approximation for periodically driven quantum systems from a Floquet-space perspective, New J. Phys. **17**, 093039 (2015).

[96] A. Lau, K. Koepernik, J. van den Brink, and C. Ortix, Generic Coexistence of Fermi Arcs and Dirac Cones on the Surface of Time-Reversal Invariant Weyl Semimetals, Phys. Rev. Lett. **119**, 076801 (2017).

[97] P. Villar Arribi, J.-X. Zhu, T. Schumann, S. Stemmer, A. A. Burkov, and O. Heinonen, Topological surface states in strained Dirac semimetal thin films, Phys. Rev. B **102**, 155141 (2020).

[98] Z. Wang, H. Weng, Q. Wu, X. Dai, and Z. Fang, Three-dimensional Dirac semimetal and quantum transport in Cd_3As_2, Phys. Rev. B **88**, 125427 (2013).

[99] S. Zhou, C. Bao, B. Fan, H. Zhou, Q. Gao, H. Zhong, T. Lin, H. Liu, P. Yu, P. Tang *et al.*, Pseudospin-selective Floquet band engineering in black phosphorus, Nature (London) **614**, 75 (2023).

[100] C. Le, S. Qin, X. Wu, X. Dai, P. Fu, C. Fang, and J. Hu, Three-dimensional topological critical Dirac semimetal in *A*MgBi (*A*=K, Rb, Cs), Phys. Rev. B **96**, 115121 (2017).

[101] A. A. Soluyanov, D. Gresch, Z. Wang, Q. Wu, M. Troyer, X. Dai, and B. A. Bernevig, Type-II Weyl semimetals, Nature (London) **527**, 495 (2015).

[102] Y. Xu, F. Zhang, and C. Zhang, Structured Weyl Points in Spin-Orbit Coupled Fermionic Superfluids, Phys. Rev. Lett. **115**, 265304 (2015).

[103] See Supplemental Material at http://link.aps.org/supplemental/10.1103/PhysRevB.107.L121407 for the Floquet Weyl semimetals and tilting effect induced by the circularly polarized light propagating along the x direction.

[104] L. Luo, H.-X. Wang, Z.-K. Lin, B. Jiang, Y. Wu, F. Li, and J.-H. Jiang, Observation of a phononic higher-order Weyl semimetal, Nat. Mater. **20**, 794 (2021).

[105] Q. Wei, X. Zhang, W. Deng, J. Lu, X. Huang, M. Yan, G. Chen, Z. Liu, and S. Jia, Higher-order topological semimetal in acoustic crystals, Nat. Mater. **20**, 812 (2021).